Supplementary Information (SI) for Chemical Science.
This journal is © The Royal Society of Chemistry 2025

Interfacial engineering of a nanofibrous Ru/Cr_2O_3 heterojunction for efficient alkaline/acid-universal hydrogen evolution at the ampere level

Xianqiang Yu[a], Mingze Xia[a], Ruikai Qi[a], Yuezhu Wang[a], Mingbin Gao[b,*], Mengxiao Zhong[c,*], Xiaofeng Lu[a,*]

[a]Alan G. MacDiarmid Institute, College of Chemistry, Jilin University, Changchun 130012, P.R. China. E-mail: xflu@jlu.edu.cn

[b]State Key Laboratory of Physical Chemistry of Solid Surfaces, College of Chemistry and Chemical Engineering, Xiamen University, Xiamen 361005, China. Email: mbgao@xmu.edu.cn

[c]State Key Laboratory of Integrated Optoelectronics, Key Laboratory of Advanced Gas Sensors, Jilin Province, College of Electronic Science and Engineering, Jilin University, Changchun, 130012 P. R. China. E-mail: zhongmx@jlu.edu.cn

EXPERIMENTAL SECTION

Materials

Poly(vinylpyrrolidone) (PVP, M_w=1300000 g mol^{-1}) and chromic acetate ($Cr(Ac)_3$) were acquired from Aladdin Chemistry Co., Ltd. Ruthenium trichloride ($RuCl_3 \cdot xH_2O$), Nafion solution (5 wt%) was supplied by Sigma-Aldrich (Shanghai). Ethanol (EtOH) and N, N-dimethylformamide (DMF) were purchased from Sinopharm Chemical Reagent Co. Ltd. Commercial Pt/C (20 wt%) was obtained from Johnson Matthey. All chemicals were used without additional purification and deionized water was used for all experiments.

Synthesis of $RuCrO_x$ NFs

The preparation of $RuCrO_x$ NFs involved an electrospinning technique coupled with a calcination process. Initially, a conventional electrospinning method was employed to prepare the $RuCl_3/Cr(Ac)_3$/PVP precursor nanofibrous membrane. In a typical experiment, $RuCl_3 \cdot xH_2O$ and $Cr(Ac)_3$ (molar ratio of 3:1 and a total mass of 0.3 g) were firstly dissolved in a mixed solvent consisting of 1.8 mL of DMF and 1.8 mL of EtOH. After the salts were completely dissolved through magnetic stirring at room temperature, 0.3 g of PVP was added into the system. Subsequently, a homogeneous

solution was obtained by continuous stirring overnight. This solution was then used directly for electrospinning under a high voltage of 18 kV and a distance of around 25 cm between the spinneret and the plane collector, then the $RuCl_3/Cr(Ac)_3$/PVP precursor nanofibrous membrane was obtained on the surface of collector. The precursor nanofibrous membrane was then placed in a muffle furnace and subjected to a calcination process at 500°C for 2 h, with a heating speed of 2°C min^{-1} in an air atmosphere. And then, the $RuCrO_x$ NFs were achieved.

Synthesis of Ru/Cr_2O_3 HNFs

The obtained $RuCrO_x$ NFs were transferred into a tubular furnace and heated under an Ar/H_2 atmosphere with a volume ratio of 95:5 at 350°C for 2 h, at a heating rate of 10°C min^{-1}. Ultimately, the Ru/Cr_2O_3 HNFs were acquired after the furnace temperature was allowed to cool down to ambient conditions. To create different control sample, the molar ratios of $RuCl_3 \cdot xH_2O$ to $Cr(Ac)_3$ in the spinning solution were varied (1:1, 2:1, and 4:1), while all other processing conditions were kept constant. These varied samples were designated as Ru/Cr_2O_3-1 HNFs, Ru/Cr_2O_3-2 HNFs and Ru/Cr_2O_3-4 HNFs, respectively.

Synthesis of Ru NFs and R-Cr_2O_3 NFs

For comparative purposes, spinning solutions composed exclusively of $RuCl_3 \cdot xH_2O$ or $Cr(Ac)_3$ were also configured. The resulting samples, following electrospinning and calcination, were designated as RuO_2 NFs and Cr_2O_3 NFs, respectively. Subsequently, these samples underwent a thermal reduction treatment in an Ar/H_2 atmosphere for 2 h. The resulting products were named as Ru NFs and R-Cr_2O_3 NFs, respectively.

Characterization

Field-emission scanning electron microscopy (FESEM, FEI Nova Nano-SEM) and transition electron microscopy (TEM, JEM-2100) were employed to explore the morphology of the as-prepared samples. High-resolution TEM (HRTEM) images, energy-dispersive X-ray (EDX) spectroscopy patterns, elemental mapping analysis, high-angle annular dark-field scanning TEM (HAADF-STEM) and selected area electron diffraction (SAED) were recorded on FEI Tecnai G2 F20. X-ray diffraction (XRD) measurement was carried out on PANalytical B.V. Empyrean with Cu Kα

radiation to ascertain the crystal structures of the as-prepared samples. X-ray photoelectron spectroscopy (XPS, Thermo Scientific ESCALAB250) was used to confirm the chemical composition of the samples. N_2 adsorption-desorption experiment was performed using AutoSorb-IQ instrument. Inductively coupled plasma-optical emission spectrometry (ICP-OES) measurement was carried out on an Agilent 725 instrument.

Electrochemical Measurements

All electrochemical tests were implemented on a CHI 760E electrochemical workstation, employing a typical three- or two-electrode configuration in either alkaline electrolyte (1 M KOH) or acidic electrolyte (0.5 M H_2SO_4). For the hydrogen evolution reaction (HER) tests, a standard three-electrode system was utilized, with a catalyst-modified carbon paper (CP) serving as the working electrode. The reference electrode consisted of Hg/HgO for alkaline electrolyte or Ag/AgCl for acidic conditions, while graphite rod was used as the counter electrode. The catalyst ink (4 mg mL^{-1}) was prepared by blending 4 mg of catalyst, 490 μL of water, 490 μL of EtOH, and 20 μL of 5 wt% Nafion solution. This ink was then coated on the CP (0.09 cm^2) via drop-casting, achieving a mass loading of 1 mg cm^{-2}. The potential measurements were referenced against a reversible hydrogen electrode (RHE), with calibration performed using the respective reference electrode (Fig. S26). According to Fig. S26, the potentials were converted to RHE using the following equation:

$$E_{RHE} = E_{Hg/HgO} + 0.918\ V$$

$$E_{RHE} = E_{Ag/AgCl} + 0.214\ V$$

Throughout the electrochemical measurement, the electrolyte was continuously purged with argon gas to ensure an inert environment. To establish a stable state for the working electrodes, several cyclic voltammetry (CV) cycles were initially performed. Linear scan voltammetry (LSV) was then conducted at a scan rate of 2 mV s^{-1} for each catalyst to evaluate its performance. Electrochemical impedance spectroscopy (EIS) was performed within a frequency range of 10^{-1}–10^5 Hz and acquired at potential of approximately −1.0 V *vs.* Hg/HgO electrode in alkaline electrolyte, or around −0.3 V *vs.* Ag/AgCl electrode in acidic electrolyte. The CV tests with various scan rates (10-

100 mV s^{-1}) were conducted within the potential window from −0.75 to −0.65 V *vs.* Hg/HgO electrode, or 0.1 to 0.2 V *vs.* Ag/AgCl electrode to determine the electrochemical double layer capacitance (C_{dl}) of the catalysts. The C_{dl} was calculated by plotting $\Delta j/2$ against the scan rate, where the slope of the linear region represents the C_{dl} value. The electrochemical active surface area (ECSA) is proportional to the C_{dl} value and can be derived using the following equation:

$$ECSA = (C_{dl} \times S)/C_s$$

Roughness factor (RF) is also calculated below:

$$RF = ECSA/S$$

The mass activities with regard to Ru in different catalysts with followed equation:

$$\text{Mass activity related to Ru } (MA_{Ru}) = j \times S/m_{Ru}$$

Turnover frequency (TOF) values were calculated as below:

$$TOF = j \times S/(z \times F \times n_{metal})$$

where C_s denotes the specific capacitance for a 1 cm^2 flat surface, which is generally considered as 0.04 mF cm^{-2}; S represents the geometric area coated by catalysts, which is 0.09 cm^2 in this work; *j* signifies the current density; m_{Ru} denotes the mass of Ru; z represents the number of electrons accepted for the generation of each H_2 molecule (2 for HER process); F represents the Faraday constant (96485.3 C mol^{-1}); n_{metal} represents the total amount of moles of all the active metal (Ru and Cr) in the catalyst.

All the aforementioned electrochemical measurements were conducted with iR compensation unless otherwise stated. For chronoamperometric measurements (i-t), the as-prepared catalysts or commercial catalysts were applied to CP with a mass loading of 2 mg cm^{-2}.

DFT calculation methods.

Periodic density functional theory (DFT) calculations were performed using the CASTEP module implemented in Material Studio. The exchange-correlation interactions were treated within the generalized gradient approximation (GGA) in the form of the Perdew-Burke-Ernzerhof (PBE) function. The van der Waals interactions were described using the empirical correction in Grimme's scheme. We used plane wave basis with a cut-off energy of 500 eV, self-consistent field (SCF) tolerance of

2×10^{-6} eV, energy 2×10^{-5} eV per atom, maximum force 0.05 eV per Å, maximum stress 0.1 GPa and maximum displacement 0.002 Å, respectively, for the geometry optimization. The Brillouin zone was sampled by (1 × 1 × 1) Monkhorst-Pack k-point mesh.

In order to avoid interactions between periodic images, a vacuum space of 15 Å was applied to all calculations. For projected density of states (PDOS) calculations, the *k*-points were set to be 4 × 2 × 1. The free energy diagram along the reaction pathway was calculated as follows:

$$\Delta G = \Delta E_{ads.} + \Delta E_{ZPE} - T\Delta S$$

where $\Delta E_{ads.}$ is the adsorption energy defined as the electronic energy difference, ΔE_{ZPE} is the change in zero-point energies, T is the temperature (298.15K) and ΔS is the entropy changes.

For the Ru/Cr_2O_3 model, the crystal plane of Ru and Cr_2O_3 is (101) and (110) plane, respectively, and these two planes are spliced into Ru/Cr_2O_3 model. The lattice mismatch rate is 5.0%. For the Ru model, the crystal plane of Ru is (101) plane. For the $RuCrO_x$ model, the (110) plane of RuO_2 is selected as model base, the ratio between Ru and Cr is 3:1, Cr is dopped into RuO_2 by replacing the Ru atoms. The vacuum layer height is 15 Å. The cell parameters of Ru/Cr_2O_3, Ru and $RuCrO_x$ are 20.0 × 12.2 × 26.0, 12.7 × 12.8 × 20.8 and 12.4 × 12.7 × 23.3. The model structures are shown in Fig. S25.

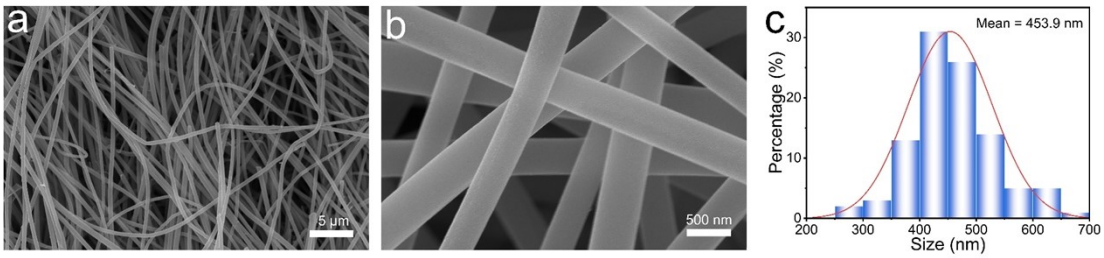

Fig. S1. SEM images of $RuCl_3/Cr(Ac)_3$-PVP precursor NFs with (a) low magnification and (b) high magnification. (c) Diameter distribution of $RuCl_3/Cr(Ac)_3$-PVP precursor NFs.

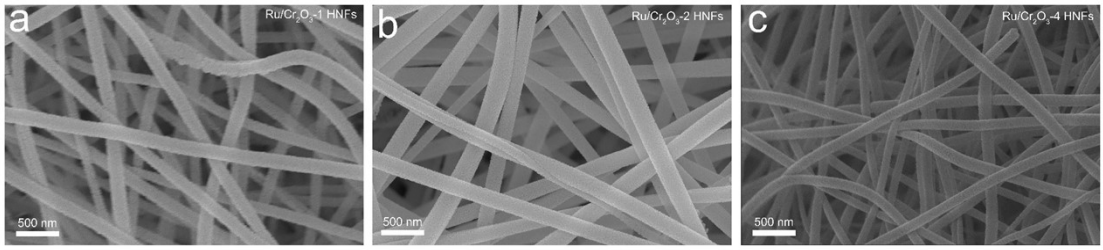

Fig. S2. SEM images of (a) Ru/Cr_2O_3-1 HNFs, (b) Ru/Cr_2O_3-2 HNFs and (c) Ru/Cr_2O_3-4 HNFs.

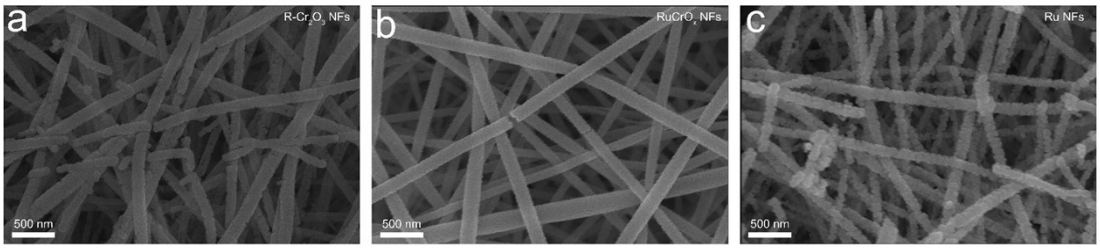

Fig. S3. SEM images of (a) R-Cr_2O_3 NFs, (b) $RuCrO_x$ NFs and (c) Ru NFs.

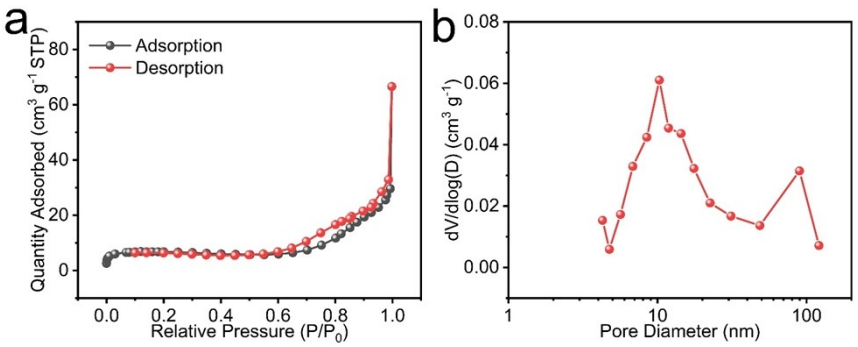

Fig. S4. (a) The N_2 adsorption-desorption isotherms and (b) corresponding pore size distribution of Ru/Cr_2O_3 HNFs.

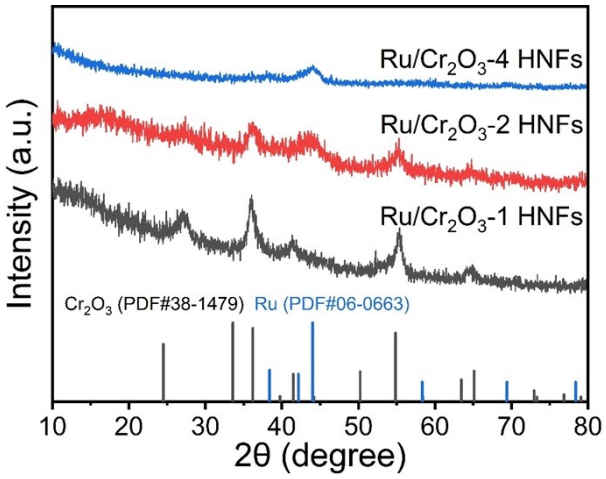

Fig. S5. XRD patterns of Ru/Cr_2O_3-1 HNFs, Ru/Cr_2O_3-2 HNFs and Ru/Cr_2O_3-4 HNFs.

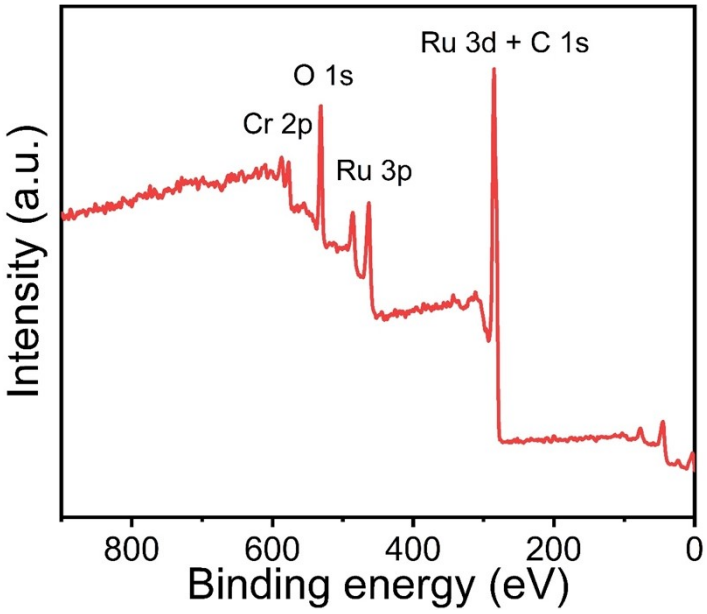

Fig. S6. XPS survey spectrum of Ru/Cr_2O_3 HNFs.

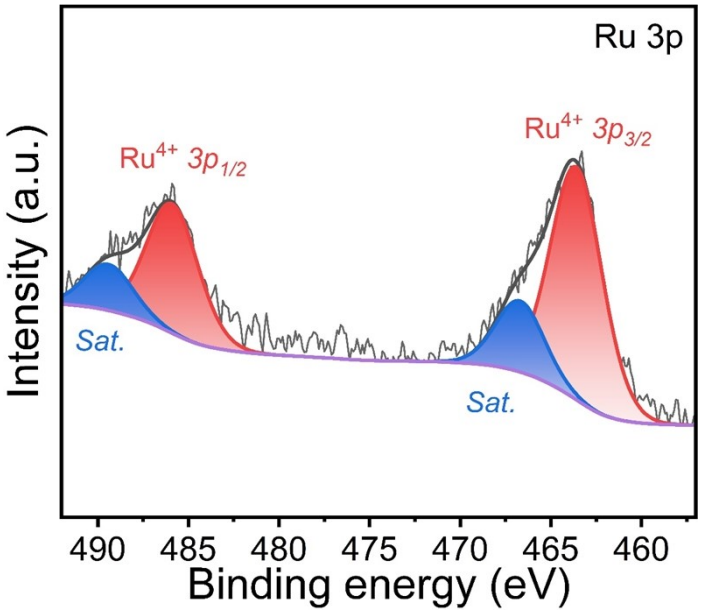

Fig. S7. Typical high-resolution Ru 3p XPS spectrum of $RuCrO_x$ NFs.

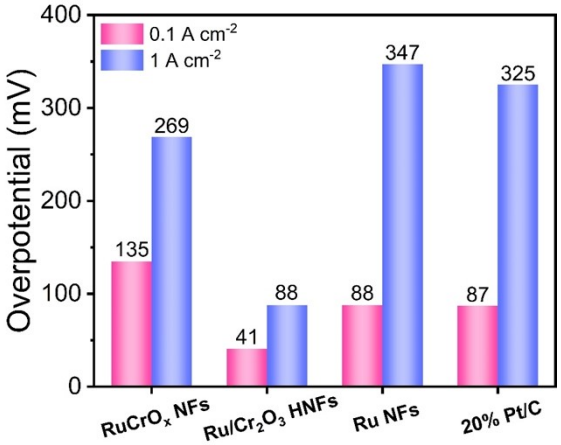

Fig. S8. Comparison of overpotentials of Ru/Cr_2O_3 HNFs and other catalysts for HER in 1 M KOH.

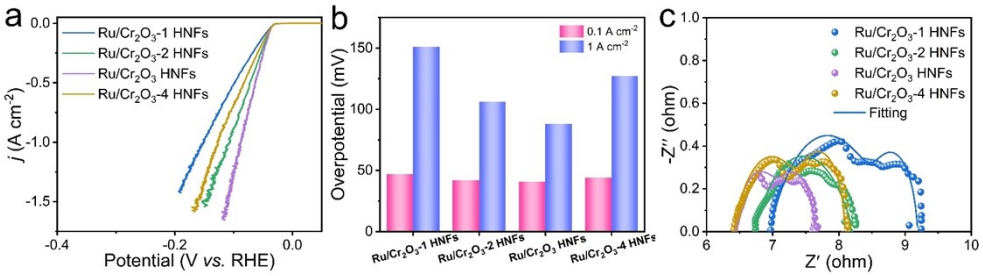

Fig. S9. Electrochemical tests of different HNFs for HER in 1 M KOH solution. (a) LSV curves, and (b) Comparison of overpotentials at 0.1 A cm^{-2} and 1 A cm^{-2} of different catalysts. (c) Nyquist plots and fitting curves at –1.0 V *versus* Hg/HgO electrode for HER.

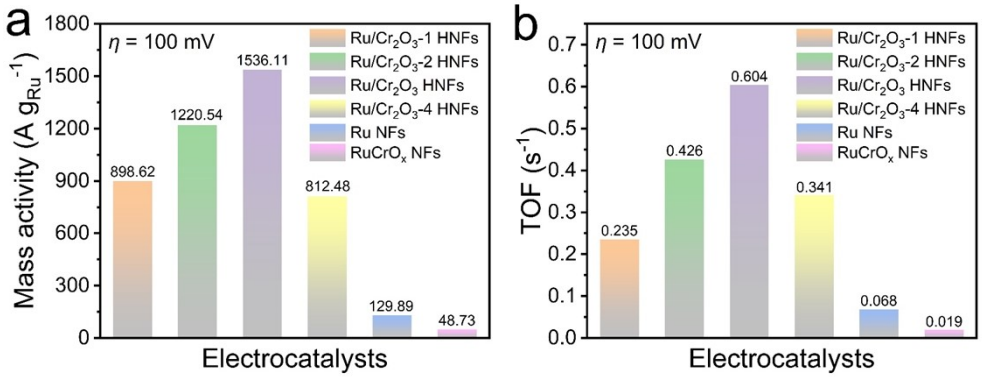

Fig. S10. Comparison of (a) the mass activities related to Ru element and (b) TOF values for Ru/Cr_2O_3 HNFs and other control catalysts toward HER process in 1 M KOH solution.

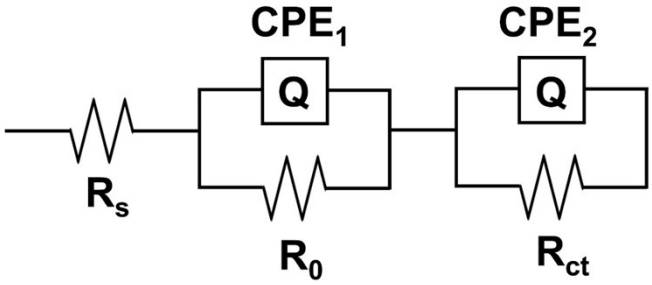

Fig. S11. The equivalent circuit model of electrodes. Where R_s is the solution resistance, CPE_1 and R_0 are the constant phase element and contact resistance between catalysts and electrode, respectively. CPE_2 is the double-layer capacitance, and R_{ct} is the charge transfer resistance at catalysts/electrolyte interface related to the HER electrocatalysis process.

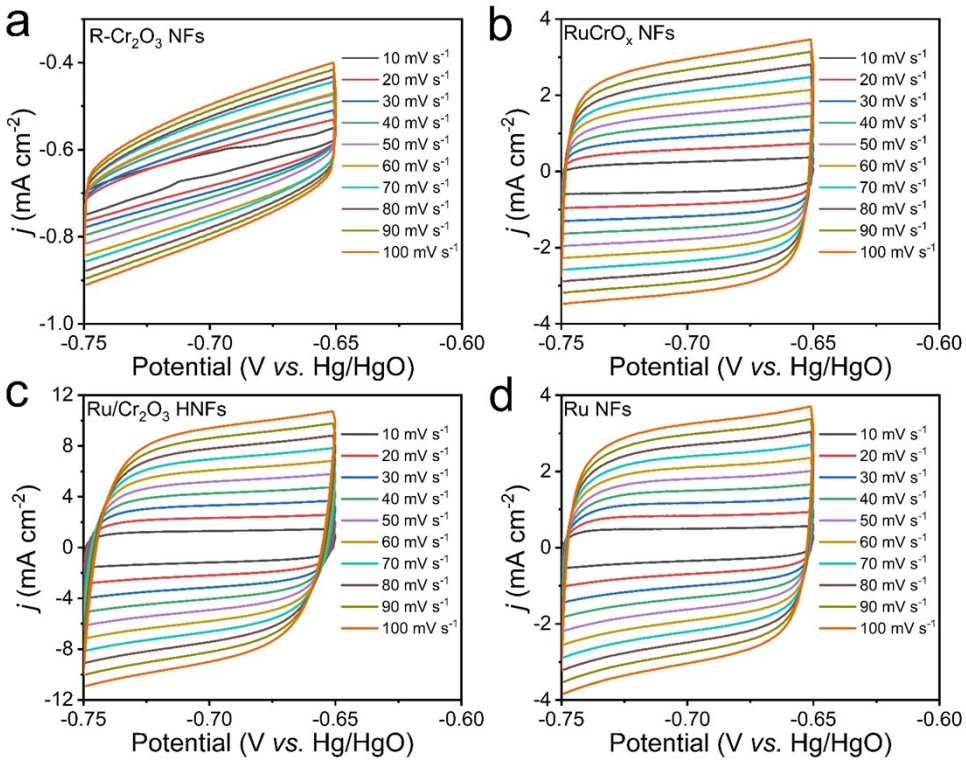

Fig. S12. The CV curves of the current density against the scan rate of (a) R-Cr_2O_3 NFs, (b) $RuCrO_x$ NFs, (c) Ru/Cr_2O_3 HNFs and (d) Ru NFs for HER in 1 M KOH solution.

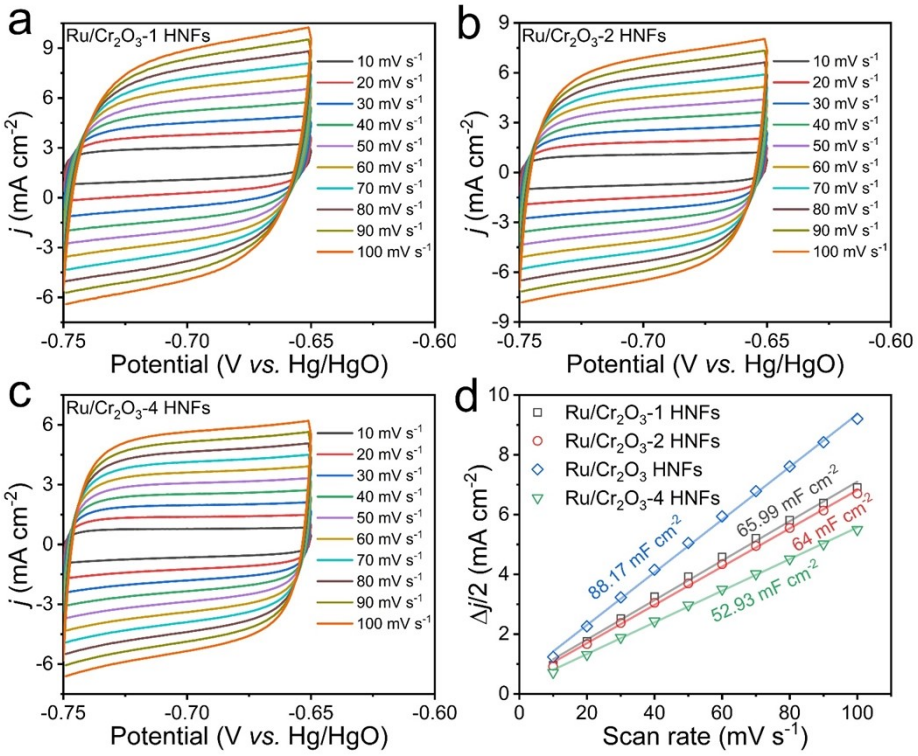

Fig. S13. The CV curves of the current density against the scan rate of (a) Ru/Cr_2O_3-1 HNFs, (b) Ru/Cr_2O_3-2 HNFs and (c) Ru/Cr_2O_3-4 HNFs for HER in 1 M KOH solution. (d) C_{dl} plots inferred from CV curves of different catalysts.

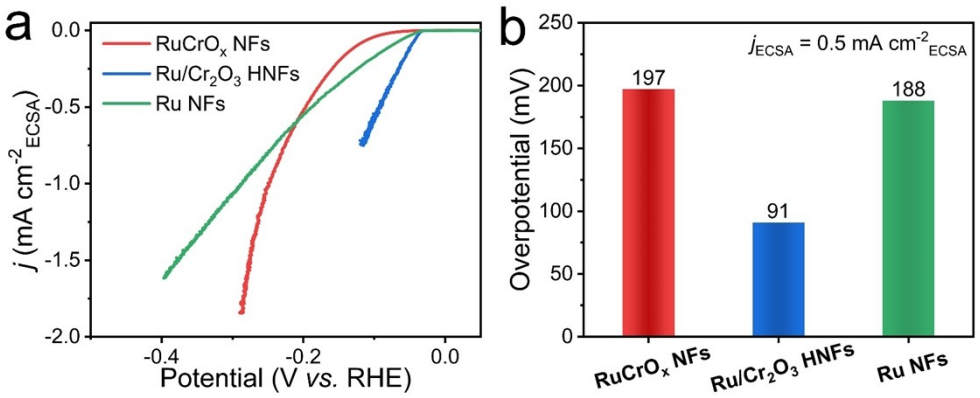

Fig. S14. (a) HER polarization curves normalized to ECSA in 1 M KOH and (b) the corresponding specific activities at the current density of 0.5 mA cm$^{-2}_{ECSA}$ of Ru/Cr_2O_3 HNFs and control catalysts.

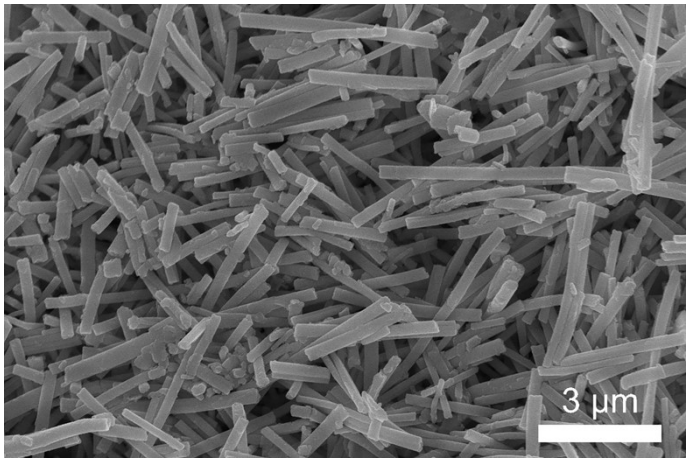

Fig. S15. SEM image of Ru/Cr_2O_3 HNFs after HER stability test in 1 M KOH solution.

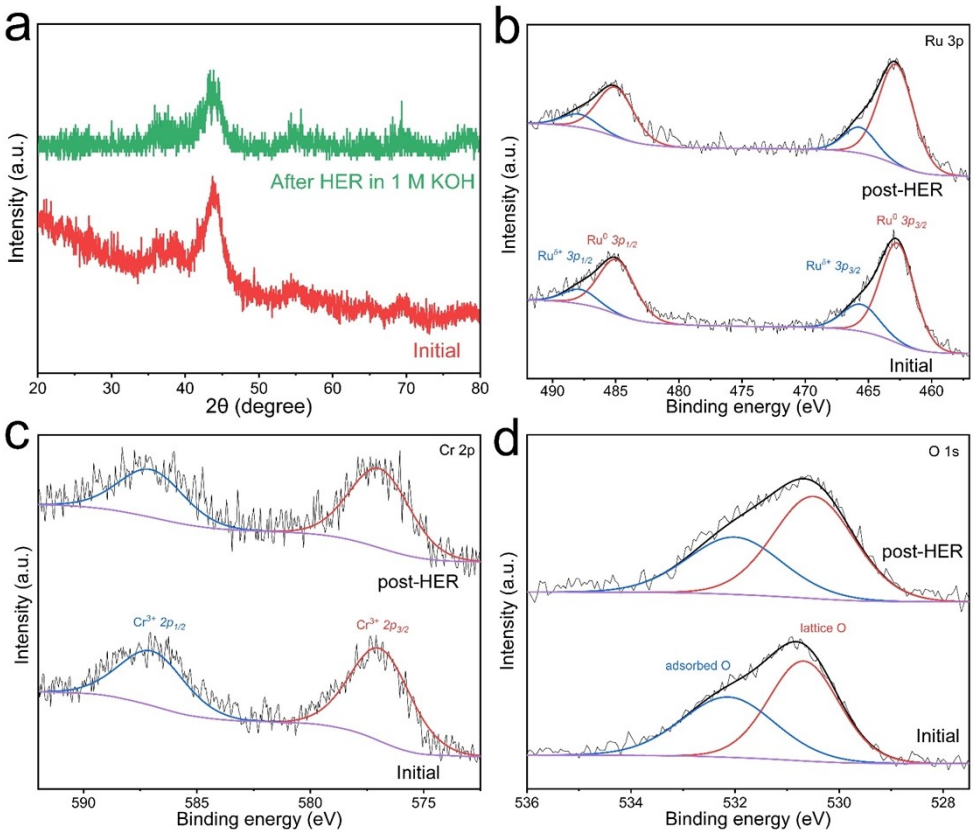

Fig. S16. (a) XRD patterns, (b) typical high-resolution Ru 3p XPS spectra, (c) typical high-resolution Cr 2p XPS spectra and (d) typical high-resolution O 1s XPS spectra of Ru/Cr_2O_3 HNFs before and after HER stability test in 1 M KOH solution.

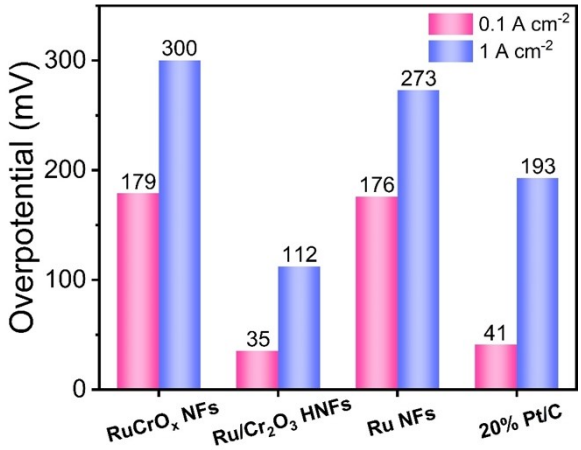

Fig. S17. Comparison of overpotentials of Ru/Cr_2O_3 HNFs and other catalysts for HER in 0.5 M H_2SO_4.

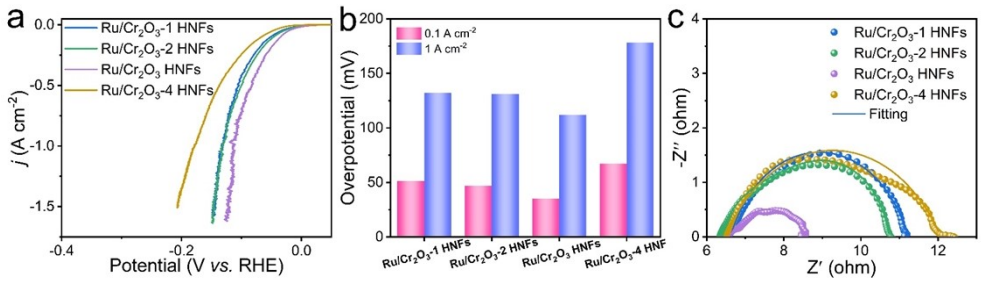

Fig. S18. Electrochemical tests of different HNFs for HER in 0.5 M H_2SO_4 solution. (a) LSV curves, and (b) Comparison of overpotentials at 0.1 A cm^{-2} and 1 A cm^{-2} of different catalysts. (c) Nyquist plots and fitting curves at –0.3 V *versus* Ag/AgCl electrode for HER.

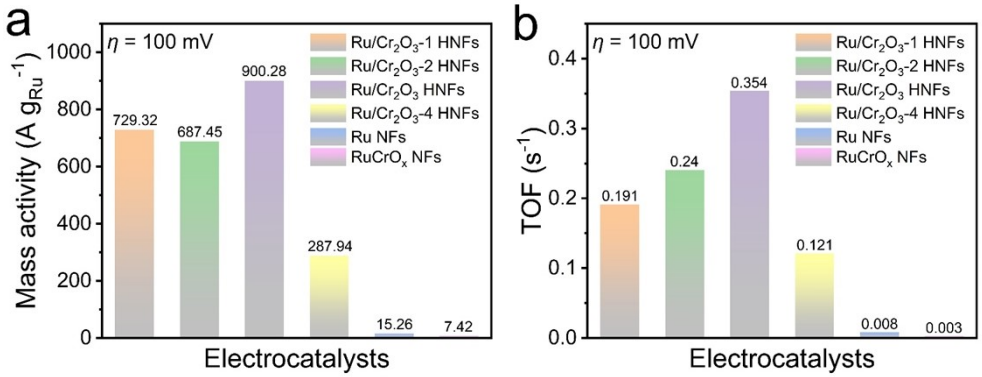

Fig. S19. Comparison of (a) the mass activities related to Ru element and (b) TOF values for Ru/Cr_2O_3 HNFs and other control catalysts toward HER process in 0.5 M H_2SO_4 solution.

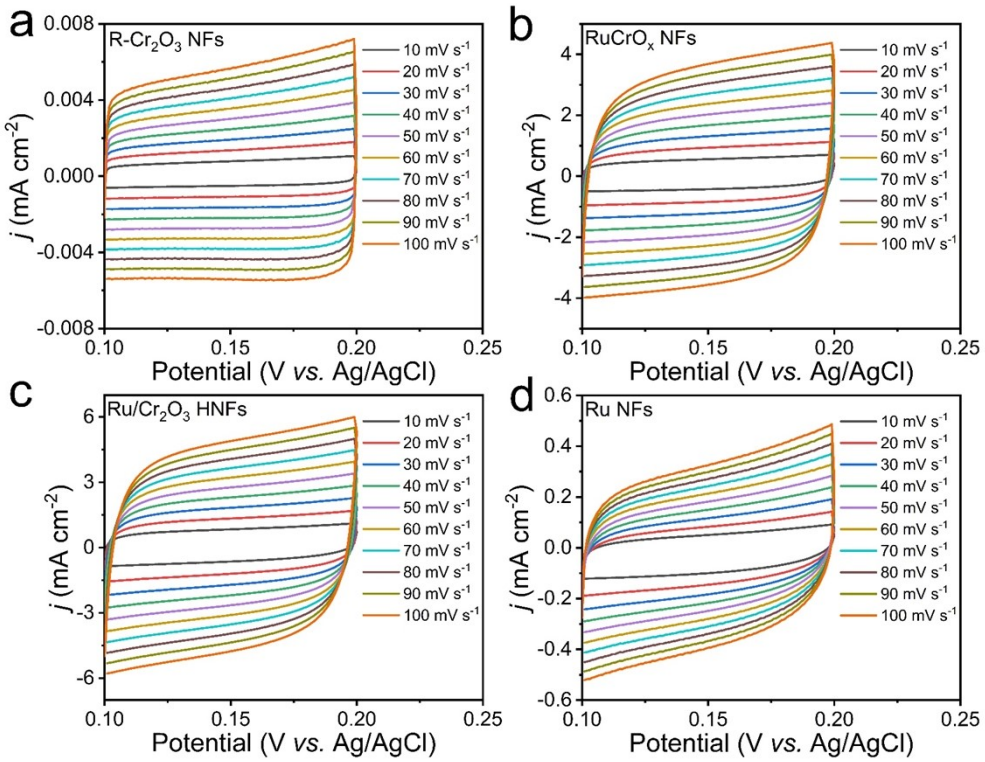

Fig. S20. The CV curves of the current density against the scan rate of (a) R-Cr_2O_3 NFs, (b) $RuCrO_x$ NFs, (c) Ru/Cr_2O_3 HNFs and (d) Ru NFs for HER in 0.5 M H_2SO_4 solution.

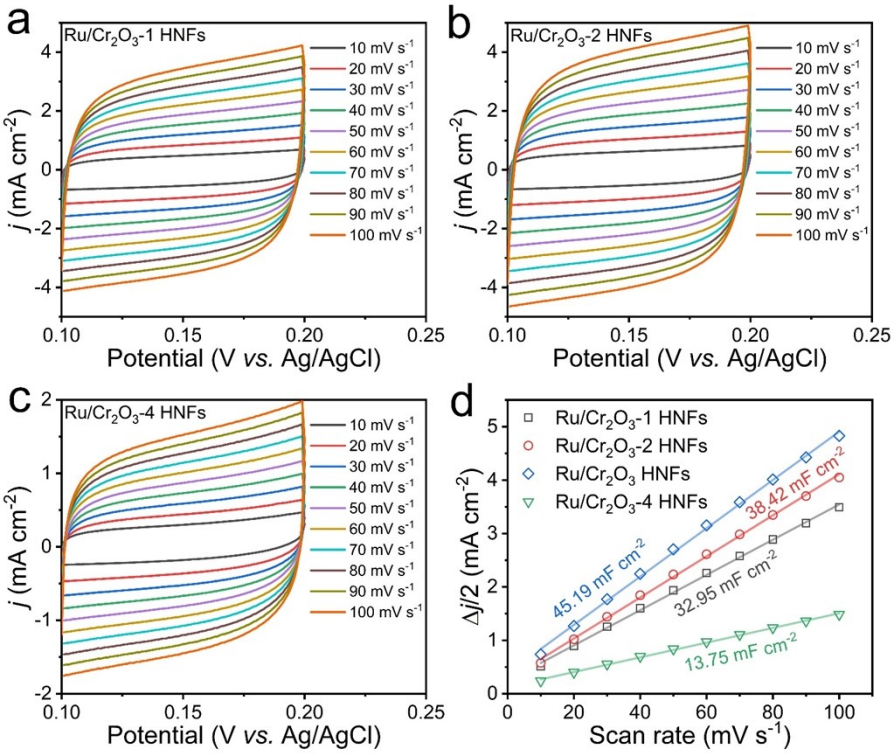

Fig. S21. The CV curves of the current density against the scan rate of (a) Ru/Cr_2O_3-1 HNFs, (b) Ru/Cr_2O_3-2 HNFs and (c) Ru/Cr_2O_3-4 HNFs for HER in 0.5 M H_2SO_4 solution. (d) C_{dl} plots inferred from CV curves of different catalysts.

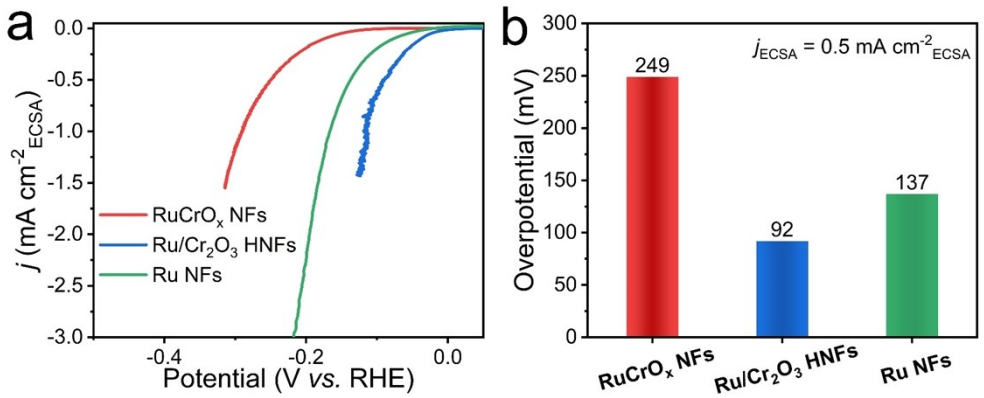

Fig. S22. (a) HER polarization curves normalized to ECSA in 0.5 M H_2SO_4 and (b) the corresponding specific activities at the current density of 0.5 mA cm^{-2}_{ECSA} of Ru/Cr_2O_3 HNFs and control catalysts.

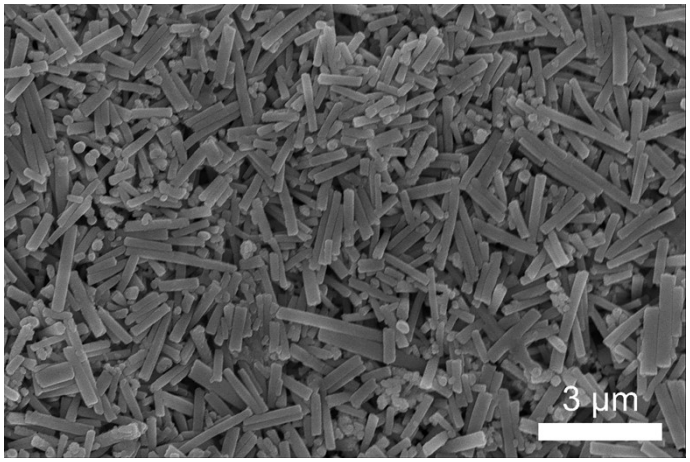

Fig. S23. SEM image of Ru/Cr_2O_3 HNFs after HER stability test in 0.5 M H_2SO_4 solution.

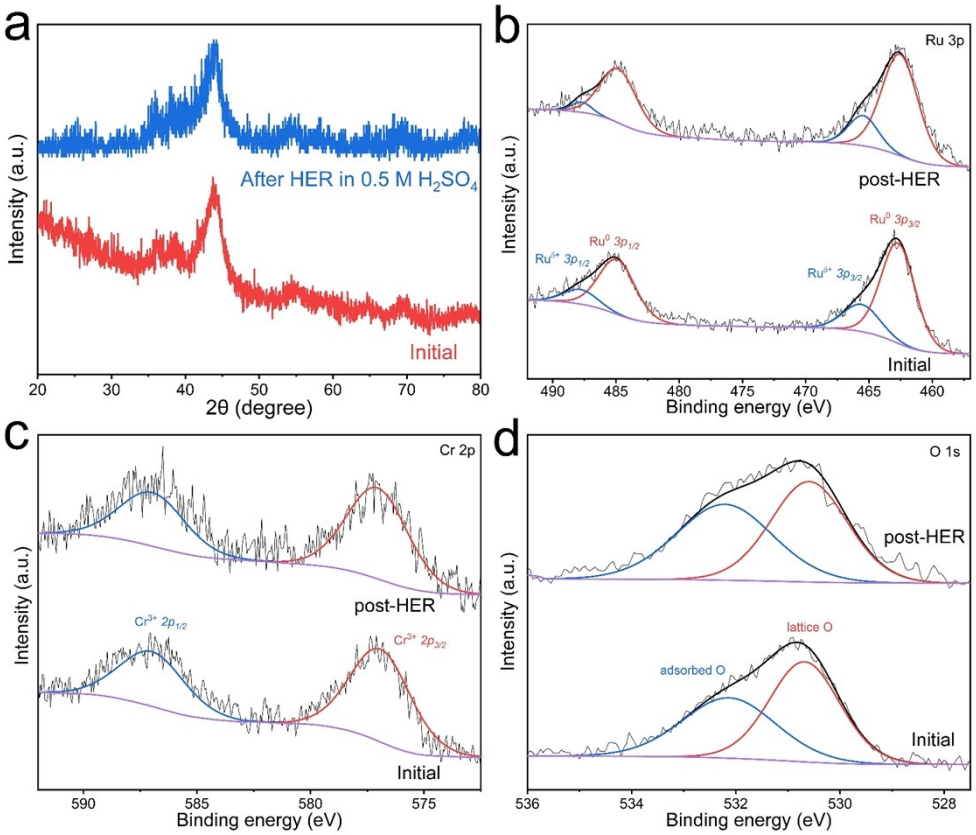

Fig. S24. (a) XRD patterns, (b) typical high-resolution Ru 3p XPS spectra, (c) typical high-resolution Cr 2p XPS spectra and (d) typical high-resolution O 1s XPS spectra of Ru/Cr_2O_3 HNFs before and after HER stability test in 0.5 M H_2SO_4 solution.

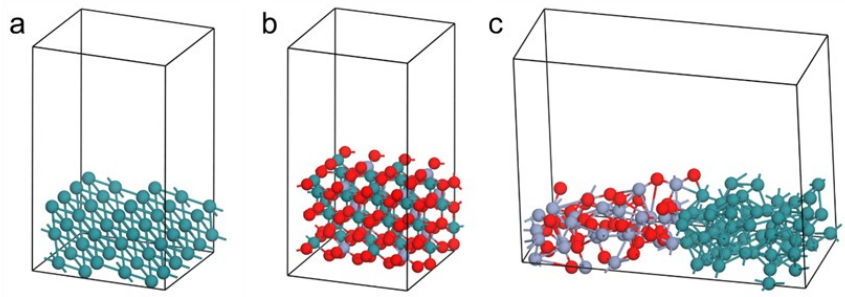

Fig. S25. The optimized models for (a) Ru(101), (b) $RuCrO_x$ and (c) Ru/Cr_2O_3.

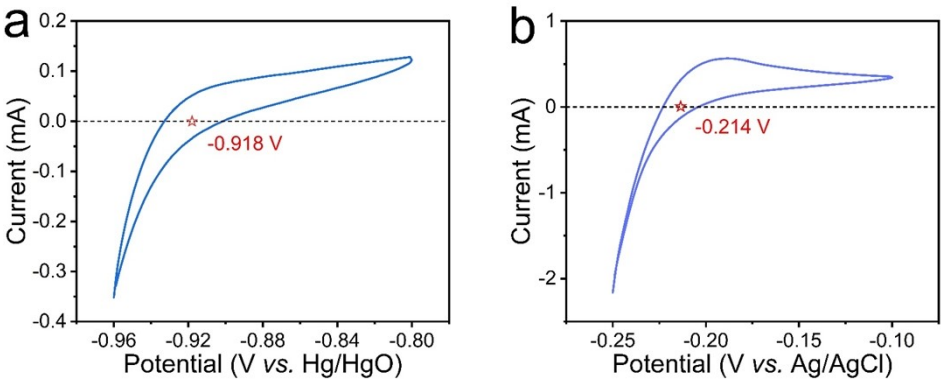

Fig. S26. The CV curves for the calibration of (a) Hg/HgO and (b) Ag/AgCl reference electrodes at the scan rate of 1 mV s^{-1} in H_2-saturated 1 M KOH solution or 0.5 M H_2SO_4 solution, respectively.

Table S1. Comparison of the HER performances among our catalyst and recently reported electrocatalysts in 1 M KOH solution.

Sample	Substrate	η@1 A cm^{-2} (mV)	Tafel slope (mV dec^{-1})	Ref.
Ru/Cr_2O_3 HNFs	CP	88	5.2	This work
Commercial Pt/C	CP	325	15.5	This work
Ru_{SAs}/$Ni(OH)_2$@FeOOH	NF	267	72	Chem. Eng. J. **2024**, 479, 147500.
V-Ru_xP_y	CP	180	21.56	Adv. Funct. Mater. **2024**, 34 (28), 2315773.
$W_{0.05}$-RuP_2@C_3N_4-NC	NF	194	84	Appl. Catal. B-Environ. **2022**, 304, 120917.
$Mn_{0.05}Ru_{0.95}O_2$ NFs	CP	269	39.2	Small. **2024**, 20 (15), 2307164.
Sr_2RuO_4	Cu wire	278	22	Nat. Commun. **2022**, 13 (1), 7784.
$Pd_4S/Pd_3P_{0.95}$	GCE	486	67.5	Adv. Energy Mater. **2022**, 12 (11), 2103511.
NA-Ru_3Ni/C	GCE	168	28	Energy Environ. Sci. **2023**, 16 (1), 285.
Pt@NiFc-MOF	NF	252	31	Adv. Funct. Mater. **2024**, 2401011.
$Ni_{9.5}Co_{0.5}$−S−FeO_x	Cu foam	230	71.4	Angew. Chem. Int. Ed. **2023**, 62 (39), e202308670.
Co_6Mo_6C-Ir-2 NFs	CP	348	96.1	Chem. Sci. **2024**, 15 (30), 11890.
$(FeCoNiB_{0.75})_{97}Pt_3$	Self-supported Ribbon	104	30.9	Adv. Mater. **2023**, 35 (38), 2303439.
Ru_{SA}@$Ti_3C_2T_x$	CC	425.7	90	EcoMat

				2023, 5 (1), e12274.

Table S2. Comparison of the C_{dl}, ECSA and RF values of Ru/Cr_2O_3 HNFs with other catalysts in 1 M KOH solution.

Catalysts	C_{dl} (mF cm^{-2})	ECSA (cm^2)	RF
Ru/Cr_2O_3-1 HNFs	65.99	148.4775	1649.75
Ru/Cr_2O_3-2 HNFs	64	144	1600
Ru/Cr_2O_3 HNFs	88.17	198.3825	2204.25
Ru/Cr_2O_3-4 HNFs	52.93	119.0925	1323.25
Ru NFs	30.06	67.635	751.5
$RuCrO_x$ NFs	29.59	66.5775	739.75
R-Cr_2O_3 NFs	1.44	3.24	36

Table S3. Comparison of the HER performances among our catalyst and recently reported electrocatalysts in 0.5 M H_2SO_4 solution.

Sample	Substrate	η@1 A cm^{-2} (mV)	Tafel slope (mV dec^{-1})	Ref.
Ru/Cr_2O_3 HNFs	CP	112	33.4	This work
Commercial Pt/C	CP	193	38.3	This work
IC-Pd@BNNTs	CP	199	35.7	Appl. Catal. B-Environ. **2024**, 345, 123609.
Pt/N-$CoWO_3$	CC	94	28	Adv. Energy Mater. **2024**, 14 (19), 2303635.
2H $Nb_{1.35}S_2$	GCE	370	38	Nat. Mater. **2019**, 18 (12), 1309.
Pt–Er/h-NC	GCE	167	17.1	J. Am. Chem. Soc. **2023**, 145 (40), 22069
Co/Se-MoS_2-NF	CP	382	67	Nat. Commun. **2020**, 11 (1), 3315.
CoRu/NC-700	GCE	227	21.4	Chem. Eng. J. **2022**, 450, 138026.
HC-MoS_2/Mo_2C	Cu foam	412	60	Nat. Commun. **2020**, 11 (1), 3724.
Co-NC-AF	Self-supported	343	67.6	Adv. Mater. **2021**, 33 (41), 2103533.
Pd_4S/$Pd_3P_{0.95}$	GCE	538	27.8	Adv. Energy Mater. **2022**, 12 (11), 2103511.
Pt-Ru/CNT	GCE	155	23	Small. **2022**, 18 (3), 2104559.
PtM/p-GO	GCE	130	23	Chem. Eng. J. **2023**, 460, 141676.
Cu-m/Cu-W/NiCo-	Cu mesh	246	79.4	Chem. Sci.

LDH				**2020**, 11 (15), 3893.
Ta-TaS_2 MC	Ta foil	≈290	30	Nat. Commun. **2021**, 12 (1), 6051.

Table S4. Comparison of the C_{dl}, ECSA and RF values of Ru/Cr_2O_3 HNFs with other catalysts in 0.5 M H_2SO_4 solution.

Catalysts	C_{dl} (mF cm^{-2})	ECSA (cm^2)	RF
Ru/Cr_2O_3-1 HNFs	32.95	74.1375	823.75
Ru/Cr_2O_3-2 HNFs	38.42	86.445	960.5
Ru/Cr_2O_3 HNFs	45.19	101.6775	1129.75
Ru/Cr_2O_3-4 HNFs	13.75	30.9375	343.75
Ru NFs	3.13	7.0425	78.25
$RuCrO_x$ NFs	34.6	77.85	865
R-Cr_2O_3 NFs	0.05	0.1125	1.25